Nonlinear Dyn (2023) 111:7773–7788
https://doi.org/10.1007/s11071-023-08235-x

ORIGINAL PAPER

Hidden extreme multistability and synchronicity of memristor-coupled non-autonomous memristive Fitzhugh–Nagumo models

Mo Chen · Xuefeng Luo · Yunhe Suo · Quan Xu · Huagan Wu

Received: 20 May 2022 / Accepted: 28 December 2022 / Published online: 14 January 2023

Abstract When taking a memristor as a coupler to connect two memristive systems, the intricate initial condition-dependent coexisting and synchronous behaviors could be achieved, which have not been comprehensively concerned in literature. This work presents a memristor-coupled homogeneous network consisting of two identical non-autonomous memristive Fitzhugh–Nagumo models and investigates its coexisting and synchronous behaviors. Kinetic analysis shows that the network can exhibit hidden extreme multistability similar to that of the individual non-autonomous memristive Fitzhugh–Nagumo model. Coexisting hidden hyperchaotic, chaotic, periodic, and quasi-periodic attractors are numerically revealed, and their synchronicities are controlled by the initial condition and coupling strength of the coupling memristor. The synchronous effects of the coupling strength and initial conditions of the network are numerically revealed using normalized mean synchronization errors. Complete and parallel-offset synchronous behaviors are realized with a large positive coupling strength and a negative initial condition of the coupling memristor. In addition to these two synchronous behaviors, phase synchronization is easily achieved due to the existence of external stimuli. These synchronous states are flexibly controlled by the initial conditions. Furthermore, an analog circuit is designed for the memristor-coupled homogenous network and circuit simulations are performed to verify the numerical results.

Keywords Homogenous network · Memristor coupler · Synchronization · Fitzhugh–Nagumo model · Hidden extreme multistability

1 Introduction

Memristor, the fourth basic circuit element described by the relationship between magnetic flux and electric charge, exhibits special nonlinear memristance or memductance nonlinearity controlled by the inner electric charge or magnetic flux variable [1]. Owing to this inner state variable, the memristor has been used as a critical building block for the construction of novel chaotic oscillating circuits [2, 3]. Various memristive circuits and systems with complex dynamical behaviors, such as self-excited or hidden extreme multistability [4, 5], multi-scroll or multi-wing chaotic attractors [6, 7], hyperchaotic attractors [8, 9], and conservative chaotic motions [10, 11], have been proposed for theoretical investigations and physical applications. The natural plasticity of memristor gives it unique advantages in simulating biological neuron synapses [12, 13] and constructing neuromorphic circuits or artificial neural networks [14, 15].

M. Chen · X. Luo · Y. Suo · Q. Xu · H. Wu (✉)
School of Microelectronics and Control Engineering, Changzhou University, Changzhou 213164, People's Republic of China
e-mail: wuhg@cczu.edu.cn

Initial condition-dependent multistability with the coexistence of multiple disconnected attractors is relatively easy to achieve in memristor-based circuits and systems. These coexisting multiple-stable states can provide great flexibility for chaos-based applications [16, 17]. Hence, exploring the synchronous control strategies and detailed synchronicities of these coexisting behaviors is of great importance. Aiming at different application requirements, researchers have proposed a variety of synchronization control strategies, including sliding mode control, impulse control, adaptive control, and finite time control, and achieved important research achievements [18–21]. Memristor shows dynamic constraint relationships among the port voltage, port current, and inner electric charge or magnetic flux variable. It can provide a new coupling synchronization scheme for nonlinear dynamical circuits and systems [22–24]. When a memristor is connected between two dynamical circuits or systems as a nonlinear coupler, the synchronization error controls its inner state variable in real time to adjust the signal exchanged between the coupled circuits or systems and promote synchronization. Some examples of such memristor-coupled networks include memristor-coupled chaotic circuits or systems [22, 23], locally active memristor-coupled neural networks [25], and memristor synapse-coupled neural networks with electromagnetic induction [26, 27].

Memristive couplers have multiple effects on the formed networks. In addition to the coupling strengths, the initial conditions of their inner state variables greatly affect the synchronization performances of the coupled networks [28, 29]. For memristor-based subsystems, the dependence of synchronous behaviors on the initial conditions of the coupled network becomes complicated. The coupling strength and initial condition of the coupling memristor and the initial conditions of the coupled subsystems exert remarkable influence on the synchronous behaviors of the memristor-coupled network. Given that the attractors of memristive systems can be offset-boosted in the phase space by the initial conditions [30], the special parallel-offset synchronization behaviors could be obtained in the memristor-coupled memristive systems [31]. However, these phenomena have not been comprehensively investigated. Therefore, this work proposes a memristor-coupled homogeneous network consisting of two identical non-autonomous memristive Fitzhugh–Nagumo models and studies its initial condition-sensitive coexisting and synchronous behaviors. The proposed network exhibits hidden extreme multistability similar to that of the individual Fitzhugh–Nagumo model. For these hidden coexisting behaviors, the complete, parallel-offset, and phase synchronization behaviors related to the coupling strength and initial conditions of the memristor-coupled network are numerically revealed and experimentally verified.

The remainder of this paper is arranged as follows. Section 2 shows the mathematical model of the proposed memristor-coupled homogeneous network and studies its equilibrium state and stability. Section 3 describes the exploration of hidden extreme multistability. Section 4 presents the investigation of coexisting synchronous behaviors. Section 5 performs PSIM (power simulation) circuit simulations to confirm the numerical simulations. Finally, Sect. 6 concludes the whole paper.

2 Mathematical models and equilibrium points

The 3D non-autonomous memristive Fitzhugh–Nagumo circuit proposed in [32] is selected as the subsystem of the coupled network. Its dimensionless mathematical model is described as

$$\begin{cases} \dot{x} = y + (a - b\tanh\varphi)x + H\cos(Ft), \\ \dot{y} = -cx - cy, \\ \dot{\varphi} = -dx. \end{cases} \tag{1}$$

An ideal memristor with smooth hyperbolic tangent memductance nonlinearity $W(\varphi) = a - b\tanh\varphi$ is adopted to implement the specific cubic nonlinearity of the Fitzhugh–Nagumo circuit. When $H\cos(Ft) \neq 0$, system (1) has no equilibrium point. When $H\cos(Ft) = 0$, the system has a line equilibrium set. With the evolution of time, the equilibrium state of system (1) switches between no equilibrium points and the line equilibrium set. For the selected system parameters $a = 0.5$, $b = 0.5$, $c = 1$, $d = 1$, $H = 1.8$, and $F = 1$, this system is proven to generate hidden extreme multistability by employing the incremental flux-charge analysis method [4].

When two identical systems as described in (1) are bidirectionally coupled by a memristor with the same smooth hyperbolic tangent memductance nonlinearity,

a 7D homogenous network can be formulated as follows

$$\begin{cases} \dot{x}_1 = y_1 + (0.5 - 0.5\tanh\varphi_1)x_1 + 1.8\cos(t) \\ \quad - k(1 - \tanh\varphi_3)(x_1 - x_2), \\ \dot{y}_1 = -x_1 - y_1, \\ \dot{\varphi}_1 = -x_1, \\ \dot{x}_2 = y_2 + (0.5 - 0.5\tanh\varphi_2)x_2 + 1.8\cos(t) \\ \quad + k(1 - \tanh\varphi_3)(x_1 - x_2), \\ \dot{y}_2 = -x_2 - y_2, \\ \dot{\varphi}_2 = -x_2, \\ \dot{\varphi}_3 = x_1 - x_2. \end{cases} \tag{2}$$

The system control parameters of the two subsystems are kept unchanged, and the kinetic and synchronous effects of coupling strength k, initial condition φ_{30} of the coupling memristor, and six initial conditions x_{10}, y_{10}, φ_{10}, x_{20}, y_{20}, and φ_{20} of the two subsystems are investigated.

Similar to the individual subsystem (1), the memristor-coupled network (2) possesses no equilibrium points for $1.8\cos(t) \neq 0$ and has a space equilibrium set $S = (0, 0, c_1, 0, 0, c_2, c_3)$ for $1.8\cos(t) = 0$. The stability of this space equilibrium set is hard to determine due to the existence of zero eigenvalues. As a solution, network (2) is reconstituted in the integral domain via incremental integral transformation [33]. With this method, the parameterized conversion of initial conditions can be achieved and the equilibrium points of the original dynamical system can be reformed to facilitate the theoretical analyses. A 4D dimensionality reduction model is then formulated as follows

$$\begin{cases} \dot{X}_1 = Y_1 + 0.5X_1 + 0.5\ln\cosh(-X_1 + \varphi_{10}) \\ \quad - 0.5\ln\cosh\varphi_{10} + 1.8\sin(t) \\ \quad - k(X_1 - X_2) + k\ln\cosh(X_1 - X_2 + \varphi_{30}) \\ \quad - k\ln\cosh\varphi_{30} + x_{10}, \\ \dot{Y}_1 = -X_1 - Y_1 + y_{10}, \\ \dot{X}_2 = Y_2 + 0.5X_2 + 0.5\ln\cosh(-X_2 + \varphi_{20}) \\ \quad - 0.5\ln\cosh\varphi_{20} + 1.8\sin(t) \\ \quad + k(X_1 - X_2) - k\ln\cosh(X_1 - X_2 + \varphi_{30}) \\ \quad + k\ln\cosh\varphi_{30} + x_{20}, \\ \dot{Y}_2 = -X_2 - Y_2 + y_{20}. \end{cases} \tag{3}$$

The state variables X_1, Y_1, X_2, and Y_2 are the incremental integrals of x_1, y_1, x_2, and y_2 in the time interval of $[0, \tau]$. The constants x_{10}, y_{10}, φ_{10}, x_{20}, y_{20}, φ_{20}, and φ_{30} indicate the seven initial conditions of network (2). Moreover, the inner state variables of the three memristors, i.e., φ_1, φ_2, and φ_3, are expressed as functions of the newly introduced state variables X_1, X_2, and their initial conditions φ_{10}, φ_{20}, and φ_{30}. Therefore, the reconstituted system (3) is reduced in dimension.

In (3), the equilibrium points of the memristor-coupled network (2) are formulated as time-varying determined equilibrium points $P = (\xi_1, y_{10} - \xi_1, \xi_2, y_{20} - \xi_2)$. The values of ξ_1 and ξ_2 are solutions of the following two equations

$$\begin{cases} -\xi_1 + \ln\cosh(-\xi_1 + \varphi_{10}) + 3.6\sin(t) - 2k(\xi_1 - \xi_2) \\ \quad + 2k\ln\cosh(\xi_1 - \xi_2 + \varphi_{30}) - 2k\ln\cosh\varphi_{30} + 2(x_{10} + y_{10}) \\ \quad - \ln\cosh\varphi_{10} = 0, \\ -\xi_2 + \ln\cosh(-\xi_2 + \varphi_{20}) + 3.6\sin(t) + 2k(\xi_1 - \xi_2) \\ \quad - 2k\ln\cosh(\xi_1 - \xi_2 + \varphi_{30}) + 2k\ln\cosh\varphi_{30} + 2(x_{20} + y_{20}) \\ \quad - \ln\cosh\varphi_{20} = 0. \end{cases} \tag{4}$$

Denoting

$$\begin{aligned} f_1 = {} & -\xi_1 + \ln\cosh(-\xi_1 + \varphi_{10}) - 2k(\xi_1 - \xi_2) \\ & + 2k\ln\cosh(\xi_1 - \xi_2 + \varphi_{30}) - 2k\ln\cosh\varphi_{30} \\ & + 2(x_{10} + y_{10}) - \ln\cosh\varphi_{10} \end{aligned} \tag{5a}$$

$$\begin{aligned} f_2 = {} & -\xi_2 + \ln\cosh(-\xi_2 + \varphi_{20}) + 2k(\xi_1 - \xi_2) \\ & - 2k\ln\cosh(\xi_1 - \xi_2 + \varphi_{30}) + 2k\ln\cosh\varphi_{30} \\ & + 2(x_{20} + y_{20}) - \ln\cosh\varphi_{20}, \end{aligned} \tag{5b}$$

and using the graphic analytic method, ξ_1 and ξ_2 are solved by inspecting the intersection points of two function curves of $f_1 + 3.6\sin(t) = 0$ and $f_2 + 3.6\sin(t) = 0$. Take $k = \pm 1$ as two examples. The curves of these two functions are depicted at $\sin(t) = 0$ and ± 1 as shown in Fig. 1. During simulations, the seven initial condition constants are specified as $x_{10} = 0.01$ and $y_{10} = \varphi_{10} = x_{20} = y_{20} = \varphi_{20} = \varphi_{30} = 0$. Note that $f_1 + 3.6\sin(t) = 0$ has no solutions when $k = 1$ and $3.6\sin(t) \to 3.6$, and $f_2 + 3.6\sin(t) = 0$ has no solutions when $k = -1$ and $3.6\sin(t) \to 3.6$. For $k > 0$, the function curves of

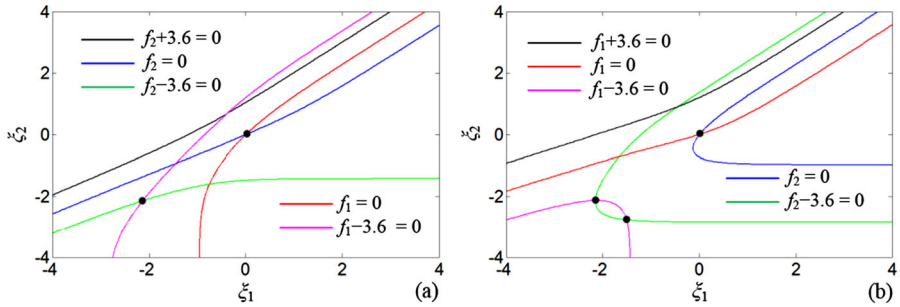

Fig. 1 Graphical representations for the intersection points of two function curves $f_1 + 3.6\sin(t) = 0$ and $f_2 + 3.6\sin(t) = 0$, **a** $k = 1$; **b** $k = -1$

$f_1 + 3.6\sin(t) = 0$ and $f_2 + 3.6\sin(t) = 0$ are monotonically increased and could have one or no intersection point, as shown in Fig. 1a. For $k < 0$, the two function curves are non-monotonically increased and may have one, two, or no intersection points as depicted in Fig. 1b.

When denoting

$$\begin{aligned} h_1 &= 0.5 - 0.5\tanh(-\xi_1 + \varphi_{10}), \\ h_2 &= 0.5 - 0.5\tanh(-\xi_2 + \varphi_{20}), \\ h_3 &= k - k\tanh(\xi_1 - \xi_2 + \varphi_{30}), \end{aligned} \tag{6}$$

the characteristic polynomial at equilibrium state P is deduced as

$$\lambda^4 + a_3\lambda^3 + a_2\lambda^2 + a_1\lambda + a_0 = 0, \tag{7}$$

with

$$\begin{aligned} a_3 &= -h_1 - h_2 + 2h_3 + 2, \\ a_2 &= h_1h_2 - h_1h_3 - h_2h_3 - 2h_1 - 2h_2 + 4h_3 + 3, \\ a_1 &= 2h_1h_2 - 2h_1h_3 - 2h_2h_3 - 2h_1 - 2h_2 + 4h_3 + 2, \\ a_0 &= h_1h_2 - h_1h_3 - h_2h_3 - h_1 - h_2 + 2h_3 + 1. \end{aligned} \tag{8}$$

If the following conditions

$$\begin{cases} a_1(a_2a_3 - a_1) - a_0a_3^2 > 0 \\ a_i > 0 \quad (i = 0,\ 1,\ 2,\ 3) \end{cases} \tag{9}$$

are all satisfied, the equilibrium points P should be stable and the generated dynamics is hidden. Given that the function tanh(•) is bounded within (− 1, 1), the three functions h_1, h_2, and h_3 in (6) are bounded within (0, 1), (0, 1), and (0, 2 k), respectively, for the positive coupling strength k. The Routh–Hurwitz criteria described in (9) are numerically evaluated within these bounded regions. The results demonstrate that all the conditions given in (9) are satisfied, indicating that the memristor-coupled network (2) maintains the hidden property of the individual system when the positive coupling strength k is assigned. For clear illustrations, the characteristics of equilibrium points for $k = -1$, 0.5, and 1 are listed in Table 1, where USF and SNF represent unstable saddle focus and stable node focus, respectively. They verify the aforementioned theoretical deductions. If the negative coupling strength k is selected, self-excited dynamical behaviors could be obtained due to the existence of unstable equilibrium points. However, numerical simulations reveal that the memristor-coupled network easily tends to be unbounded when the negative coupling strength k is chosen.

3 Hidden extreme multistability of the memristor-coupled homogenous network

This section discusses the hidden extreme multistability of the memristor-coupled homogenous network. The differential equations of network (2) are solved using the MATLAB ODE45 algorithm with a time step of 0.01, and the Lyapunov exponents (LEs) are calculated by the ODE45-based Wolf's Jacobian matrix method.

3.1 Coexisting behaviors induced by the coupling memristor

The coexisting behaviors induced by the coupling memristor are examined by taking coupling strength k and initial condition φ_{30} as two varying parameters. The initial conditions of the two subsystems are fixed as $(x_{10}, y_{10}, \varphi_{10}, x_{20}, y_{20}, \varphi_{20}) = (0.01, 0, 0, 0, 0, 0)$. The varying parameters k and φ_{30} are adjusted in the regions of [− 0.05, 0.2] and [− 1, 6], respectively.

The 2D bifurcation diagram of network (2) is plotted in Fig. 2a by checking the periodicities of state

Table 1 Characteristics of reformed equilibrium points for different values of k

k	3.6sin(t)	Coordinates	Eigenvalues	Stabilities
− 1	− 3.6	(− 2.1395, 2.1395, − 2.1297, 2.1297)	$\lambda_1 = 1.6570$, $\lambda_{2,3} = -0.4931 \pm j0.8620$, $\lambda_4 = -0.6236$	USF
		(− 1.4954,1.4954, − 2.7615, 2.7615)	$\lambda_{1,2} = -0.3390 \pm j0.7504$, $\lambda_{3,4} = -0.4879 \pm j0.8589$	SNF
	− 1.8	(− 1.2026, 1.2026, − 1.1935, 1.1935)	$\lambda_1 = 1.7362$, $\lambda_{2,3} = -0.4583 \pm j0.8405$, $\lambda_4 = -0.6345$	USF
		(− 0.4149, 0.4149, − 1.8756, 1.8756)	$\lambda_{1,2} = -0.2804 \pm j0.6944$, $\lambda_{3,4} = -0.4541 \pm j0.8378$	SNF
	0	(0.0067, − 0.0067, 0.0134, − 0.0134)	$\lambda_1 = 2.2066$, $\lambda_{2,3} = -0.2475 \pm j0.6586$, $\lambda_4 = -0.6881$	USF
	1.8	No equilibrium point	–	–
	3.6	No equilibrium point	–	–
0.5	− 3.6	(− 2.1321, 2.1321, − 2.1372, 2.1372)	$\lambda_{1,2} = -0.4931 \pm j0.8620$, $\lambda_{3,4} = -0.9906 \pm j1.0000$	SNF
	− 1.8	(− 1.1954, 1.1954, − 1.2006, 1.2006)	$\lambda_{1,2} = -0.4583 \pm j0.8405$, $\lambda_{3,4} = -0.9557 \pm j0.9990$	SNF
	0	(0.0134, − 0.0134, 0.0067, − 0.0067)	$\lambda_{1,2} = -0.2475 \pm j0.6586$, $\lambda_{3,4} = -0.7441 \pm j0.9667$	SNF
	1.8	No equilibrium point	–	–
	3.6	No equilibrium point	–	–
1	− 3.6	(− 2.1329, 2.1329, − 2.1363, 2.1363)	$\lambda_{1,2} = -0.4931 \pm j0.8620$, $\lambda_{3,4} = -1.4897 \pm j0.8719$	SNF
	− 1.8	(− 1.1963, 1.1963, − 1.1997, 1.1997)	$\lambda_{1,2} = -0.4583 \pm j0.8405$, $\lambda_{3,4} = -1.4549 \pm j0.8906$	SNF
	0	(0.0121, − 0.0121, 0.0080, − 0.0080)	$\lambda_{1,2} = -1.2434 \pm j0.9699$, $\lambda_{3,4} = -0.2475 \pm j0.6586$	SNF
	1.8	No equilibrium point	–	–
	3.6	No equilibrium point	–	–

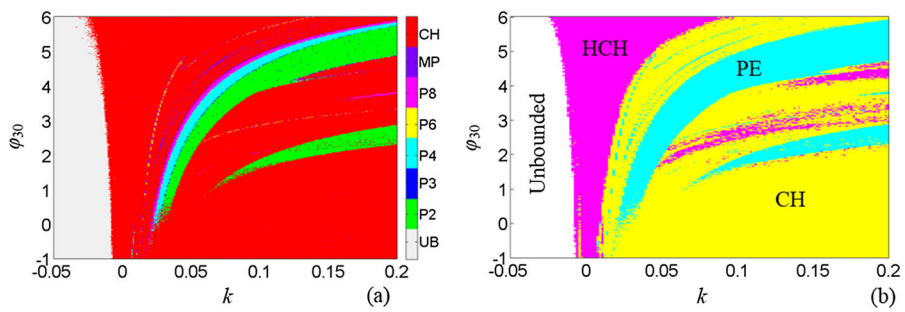

Fig. 2 Bifurcation plots in the k-φ_{30} plane with fixed subsystems' initial conditions (x_{10}, y_{10}, φ_{10}, x_{20}, y_{20}, φ_{20}) = (0.01, 0, 0, 0, 0, 0), **a** 2D bifurcation diagram, **b** distributions of dynamical behaviors distinguished by the sign of LEs

variable φ_1. The chaotic (CH), periodic, and unbounded (UB) behaviors are indicated by different colors. The labels P2, P3, P4, P6, and P8 represent periodic behaviors with different periodicities. The label MP represents the multi-period behaviors, whose periodicities are between 9 and 15. If the periodicity goes beyond 15, the corresponding dynamical behaviors are identified as chaotic ones and labeled as CH in Fig. 2a. Meanwhile, the dynamical regions in the k-φ_{30} plane are further distinguished by the signs of LEs and illustrated in Fig. 2b for intuitive comparisons. In Fig. 2b, the periodic (PE) region covers the P2 to MP regions of Fig. 2a. The hyperchaotic (HCH) behaviors, which have two positive, three zero, and two negative LEs, are distinguished from the chaotic ones. The dynamical patterns in Fig. 2a, b match well with each other. In the 2D bifurcation diagram of Fig. 2a, the hyperchaotic and chaotic behaviors are not distinguished from each other and the periodic phenomena that only occur in extremely narrow parameter regions are not displayed. The 2D bifurcation plots given in later sections follow the same principle.

As shown in Fig. 2, the homogeneous network easily goes infinite when the negative k is assigned. If

the two subsystems are weakly coupled, hyperchaotic behaviors tend to occur. The chaotic or periodic behaviors emerge as the positive coupling strength k increases gradually. $k = 0.05$ and 0.2 are taken as the representative cases to explore the detailed bifurcation behaviors induced by the coupling memristor coefficients. The 1D bifurcation diagrams (top) and the corresponding first four LE spectra (bottom) are presented in Fig. 3. The hyperchaotic, chaotic, and periodic behaviors and the period-doubling bifurcation, tangential bifurcation, and crisis scenarios, are illustrated. They further verify the dynamical evolution characteristics revealed in Fig. 2.

As φ_{30} approaches 0 or becomes negative, the bifurcation plots of φ_1 and φ_2 tend to overlap. Meanwhile, the bifurcation plot of φ_3 tends to be constant. According to the seventh equation of (2), the time derivation of φ_3 equals the difference between x_1 and x_2, indicating that φ_3 tends to be constant when the two subsystems reach complete synchronization, i.e., $x_1 - x_2 = 0$. These phenomena indicate that the two subsystems can achieve complete synchronization for small or negative φ_{30} when a positive k is selected. This synchronous region becomes enlarged with the increase of the coupling strength k.

Take $k = 0.2$ as an example. Four different sets of phase diagrams and time-domain waveforms are plotted in Fig. 4 for $\varphi_{30} = -1$, 2.5, 3.5, and 4.8. Figure 4a shows the chaotic motions at $\varphi_{30} = -1$ with one positive, three zero, and three negative LEs. In this case, the phase trajectories and time-domain waveforms of the two subsystems fit together, indicating the generation of completely synchronized chaotic motions. Figure 4b exhibits asynchronous periodic behavior at $\varphi_{30} = 2.5$ with three zero and four negative LEs; Fig. 4c displays asynchronous hyperchaotic behavior at $\varphi_{30} = 3.5$ with two positive, three zero, and two negative LEs; and Fig. 4d shows asynchronous quasi-periodic behavior at $\varphi_{30} = 4.8$ with four zero and three negative LEs. For $\varphi_{30} = 3.5$, the memristor-coupled network reaches complete synchronization in partial periods, as illustrated by the time-domain waveforms in Fig. 4c.

3.2 Coexisting behaviors induced by the subsystems' initial conditions

The coexisting behaviors induced by the initial conditions of the two subsystems are examined by setting the coupling memristor-related coefficients as $k = 0.2$ and $\varphi_{30} = 0$. The subsystems' initial conditions are set as (x_{10}, 0, φ_{10}, 0, 0, 0), and the examined initial conditions x_{10} and φ_{10} are varied in the range of $[-1, 1]$.

The 2D bifurcation plot in the x_{10}-φ_{10} plane is depicted in Fig. 5a. The chaotic (red) and periodic (magenta, yellow, blue, light blue, and green) behaviors with different topological structures or locations coexist in the memristor-based homogenous network. In addition, Fig. 5b displays the 2D bifurcation plot in the φ_{10}-φ_{20} plane for the subsystems' initial conditions (0.01, 0, φ_{10}, 0, 0, φ_{20}). It also reveals coexisting chaotic and periodic behaviors with different topological structures or locations. Similar to Fig. 2a, the coexisting phenomena that occur only in extremely narrow initial condition regions are ignored in Fig. 5.

Corresponding to Fig. 5a, the representative phase portraits for coexisting attractors with varied x_{10} and fixed $\varphi_{10} = 0$ are plotted in Fig. 6a. Meanwhile, the representative phase portraits for coexisting attractors of Fig. 5b are depicted in Fig. 6b with varied φ_{10} and fixed $\varphi_{20} = 0$. With the variation of initial condition

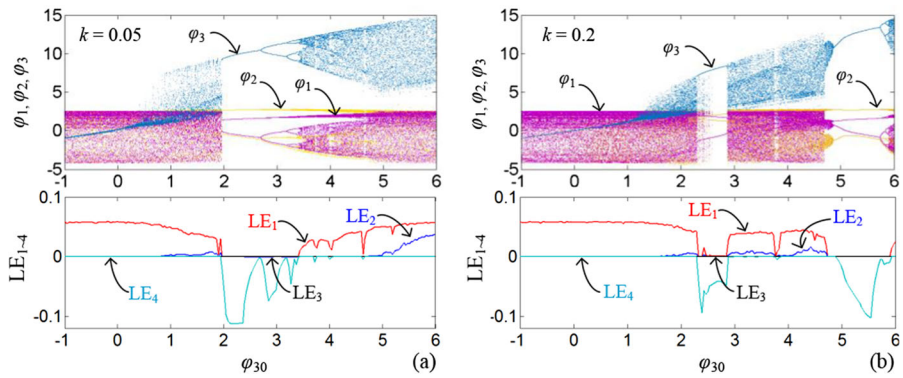

Fig. 3 1D bifurcation plots induced by φ_{30} with fixed subsystems' initial conditions (x_{10}, y_{10}, φ_{10}, x_{20}, y_{20}, φ_{20}) = (0.01, 0, 0, 0, 0, 0), **a** $k = 0.05$, **b** $k = 0.2$

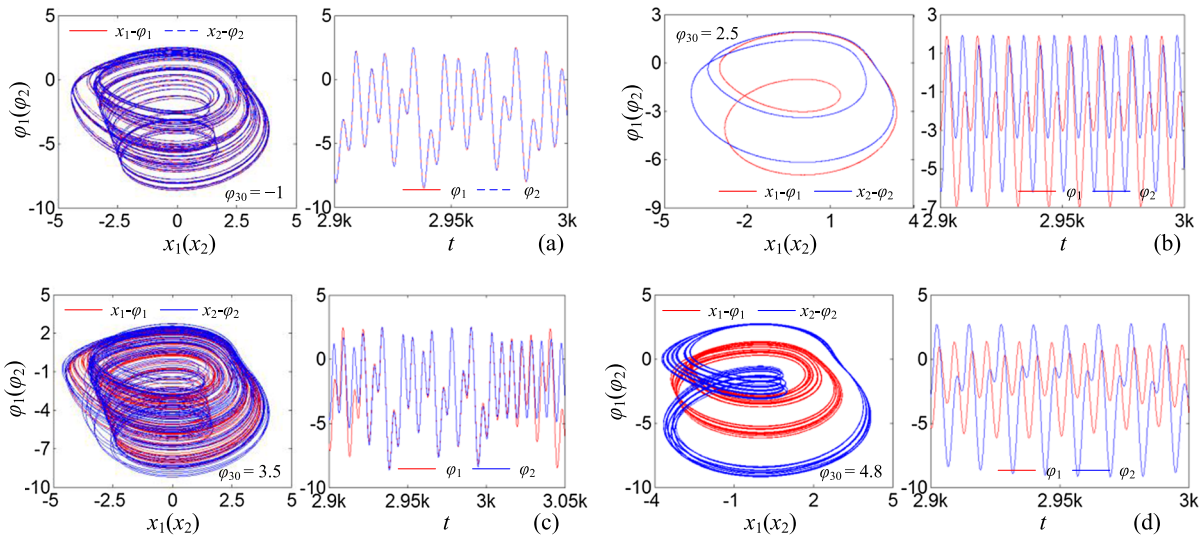

Fig. 4 Phase portraits in the x_1-φ_1 and x_2-φ_2 planes for the representative dynamical behaviors with fixed subsystems' initial conditions (x_{10}, y_{10}, φ_{10}, x_{20}, y_{20}, φ_{20}) = (0.01, 0, 0, 0, 0, 0) and coupling strength k = 0.2, **a** $\varphi_{30} = -1$, **b** φ_{30} = 2.5, **c** φ_{30} = 3.5, **d** φ_{30} = 4.8

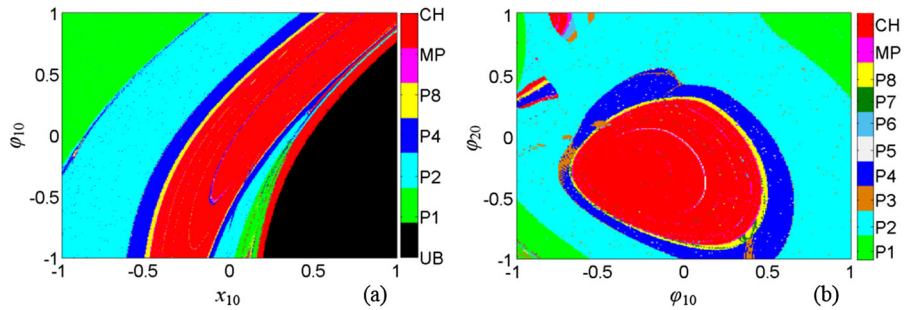

Fig. 5 2D bifurcation plots induced by the subsystems' initial conditions with fixed k = 0.2 and φ_{30} = 0, **a** 2D bifurcation plot in the x_{10}-φ_{10} plane for (x_{10}, 0, φ_{10}, 0, 0, 0), **b** 2D bifurcation plot in the φ_{10}-φ_{20} plane for (0.01, 0, φ_{10}, 0, 0, φ_{20})

x_{10} or φ_{10}, the dynamical behaviors of two subsystems are changed. Moreover, the attractor position of the first subsystem shifts along the φ_1-coordinate, as reflected by the relative positions between the red (subsystem 1) and blue (subsystem 2) trajectories. This phenomenon may be related to the space equilibrium set S = (0, 0, c_1, 0, 0, c_2, c_3) that exists at $H\cos(Ft)$ = 0. For dynamical systems with the line or space equilibrium sets, the generated attractors are located around one nearby equilibrium point around the assigned initial conditions. Correspondingly, the generated attractors move along the axis or plane where the equilibrium points are located. However, in network (2), the equilibrium state switches between a space equilibrium set and no equilibrium points because the stimulus $H\cos(Ft)$ is not always equal to zero. Thus, the cause of attractors' displacement cannot be explicitly identified and still needs further exploration.

The dynamics of the memristor-coupled homogeneous network is flexibly controlled by the initial conditions of the coupling memristor and two subsystems. In particular, the complete period-doubling bifurcation routes are found with the variations of x_{10}, φ_{10}, φ_{20}, and φ_{30}, leading to the generation of hidden extreme multistability [34] with infinite hidden coexisting attractors. The detailed synchronous behaviors of these coexisting attractors are discussed in Sect. 4.

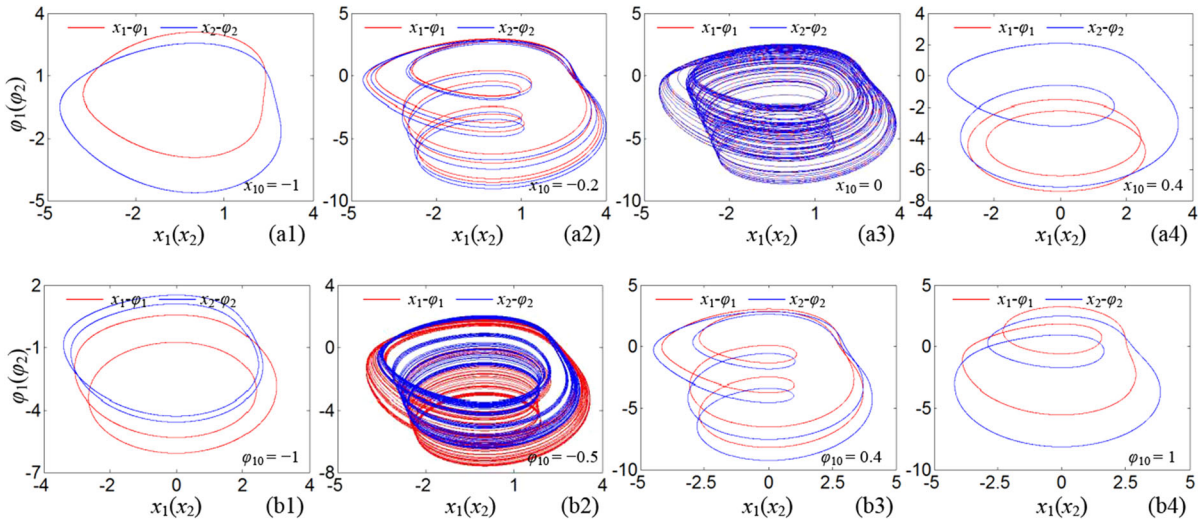

Fig. 6 Phase portraits in the $x_1(x_2)$ -$\varphi_1(\varphi_2)$ planes for the coexisting attractors induced by the subsystems' initial conditions with fixed k = 0.2 and φ_{30} = 0, **a** x_{10} = − 1, − 0.2, 0, and 0.4 for (x_{10}, 0, 0, 0, 0, 0), **b** φ_{10} = − 1, − 0.5, 0.4, and 1 for (0.01, 0, φ_{10}, 0, 0, 0)

4 Synchronous behaviors of the memristor-coupled homogenous network

This section depicts the synchronicities of the memristor-coupled homogenous network (2) using several numerical measures.

4.1 Complete synchronization

As revealed in Figs. 3 and 4, the memristor-coupled network (2) can achieve complete synchronization states when only a minor initial condition mismatch occurs between the two subsystems. In this case, the synchronization error of two subsystems is quantitatively evaluated using the normalized mean synchronization error [28, 35] defined as

$$E = \frac{1}{N}\sum_{n=1}^{N}\frac{\sqrt{[x_1(n)-x_2(n)]^2+[y_1(n)-y_2(n)]^2+[\varphi_1(n)-\varphi_2(n)]^2}}{\sqrt{x_1(n)^2+y_1(n)^2+\varphi_1(n)^2+x_2(n)^2+y_2(n)^2+\varphi_2(n)^2}} \tag{10}$$

where $x_j(n)$, $y_j(n)$, and $\varphi_j(n)$ (j = 1, 2) are the sampling values of state variables within a certain time interval. N samples are used to calculate the normalized mean synchronization error. If E approaches 0, complete synchronization is realized.

For the fixed subsystems' initial conditions (x_{10}, y_{10}, φ_{10}, x_{20}, y_{20}, φ_{20}) = (0.01, 0, 0, 0, 0, 0), the normalized mean synchronization errors in the k-φ_{30} plane are calculated using the data samples within the time interval of [3900, 4000]. The obtained results are presented in Fig. 7a. The red area indicates that the normalized mean synchronization error E is close to 0 and the complete synchronization state is achieved. The other colored areas indicate that E is positive and the two coupled subsystems are out of synchronization. We can find that the memristor-coupled network (2) realizes complete synchronization with a larger positive coupling strength k and a more negative memristor initial condition φ_{30}.

As revealed in Figs. 5 and 6, infinite coexisting attractors controlled by the subsystems' initial conditions are observed in the memristor-coupled homogenous network. Their synchronization states are of particular interest for understanding the synchronicities of memristor-coupled network (2). For coexisting attractors revealed in Fig. 5a, the normalized mean synchronization errors in the x_{10}-φ_{10} plane are presented in Fig. 7b. Network (2) can reach complete synchronization when the initial conditions x_{10} and φ_{10} are located in the red region nearby the diagonal line. The non-memristor initial condition x_{10} and memristor initial condition φ_{10} show different shifting effects on the phase space positions of the generated attractors [36]. Their shifting effects cancel each other out when x_{10} and φ_{10} are properly tuned. For example, if x_{10} is specified as − 0.8, − 0.5, and − 0.2, zero E can be achieved by optimizing φ_{10} as − 0.93, − 0.57, and − 0.226, respectively. Therefore,

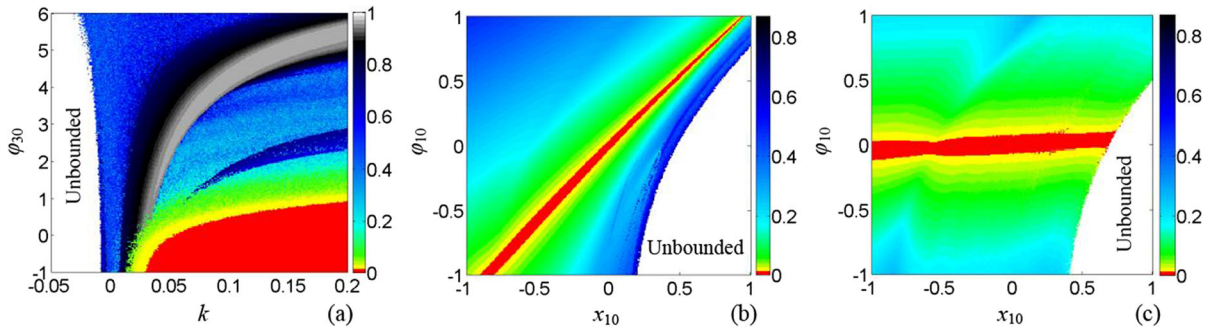

Fig. 7 The complete synchronization areas depicted by the normalized mean synchronization error E, **a** the distribution of E in the k-φ_{30} plane for (x_{10}, y_{10}, φ_{10}, x_{20}, y_{20}, φ_{20}) = (0.01, 0, 0, 0, 0, 0), **b** the distribution of E in the x_{10}-φ_{10} plane for (x_{10}, 0, φ_{10}, 0, 0, 0), k = 0.2 and φ_{30} = 0, **c** the distribution of E in the x_{10}-φ_{10} plane for (x_{10}, 0, φ_{10}, 0, 0, 0), k = 5 and φ_{30} = − 5

completely synchronized periodic and chaotic motions can be obtained.

However, when large positive coupling strengths and negative coupling memristor initial conditions are selected, i.e., k = 5 and φ_{30} = − 5, the synchronization error significantly decreases as illustrated in Fig. 7c. The red complete synchronization region in the x_{10}-φ_{10} plane migrates to the vicinity of φ_{10} = 0 and its scope is slightly expanded. This finding further verifies the synchronous effects of the coupling memristor coefficients.

4.2 Parallel-offset synchronization

In addition to the complete synchronization behaviors, parallel-offset synchronization behaviors could be expected, that is, the state variables $x_1(x_2)$ and $y_1(y_2)$ fit each other perfectly but the state variables φ_1 and φ_2 oscillate synchronously with a certain position offset determined by the initial condition mismatches between the two subsystems. The synchronization errors of the non-memristor state variables $x_1(x_2)$ and $y_1(y_2)$ can be evaluated by the normalized mean synchronization error E' defined as

$$E' = \frac{1}{N}\sum_{n=1}^{N}\frac{\sqrt{[x_1(n)-x_2(n)]^2+[y_1(n)-y_2(n)]^2}}{\sqrt{x_1(n)^2+y_1(n)^2+x_2(n)^2+y_2(n)^2}} \tag{11}$$

The parallel-offset synchronization behaviors are examined by comparing the normalized mean synchronization errors E and E'.

When the subsystems' initial conditions are fixed as (x_{10}, y_{10}, φ_{10}, x_{20}, y_{20}, φ_{20}) = (0.01, 0, 0.3, 0, 0, 0), initial condition mismatches are observed between the two subsystems. Figure 8a displays the 1D plots of E and E' depicted within k = [0, 5] for φ_{30} = 0 and − 5, and Fig. 8b presents the 1D plots of E and E' depicted within φ_{30} = [− 5, 4] for k = 0.2 and 5. For fixed φ_{30} = 0 and − 5, E tends to be a nonzero constant, and E' gradually reaches 0 with the increase of k. When the positive coupling strength k is large enough, the error between state variables $x_1(x_2)$ and $y_1(y_2)$ asymptotically approaches zero and that between φ_1 and φ_2 oscillates around a constant. This finding indicates the generation of parallel-offset synchronization. The synchronization error between $x_1(x_2)$ and $y_1(y_2)$ continuously decreases with the increase of k. For fixed k = 0.2 and 5 in Fig. 8b, the memristor-coupled network enters a parallel-offset synchronization state when φ_{30} decreases below a certain threshold. Afterward, φ_{30} no longer has a significant influence on the synchronization errors.

In Fig. 9a, the distribution of E' in the x_{10}-φ_{10} plane is depicted with fixed k = 5 and φ_{30} = − 5. It demonstrates the parallel-offset synchronization regions in the x_{10}-φ_{10} plane when initial condition mismatches occur between the two subsystems. Note that the complete synchronization is a special case of the parallel-offset synchronization. Excluding the red complete synchronization regions depicted in Fig. 7c, the remaining blue regions can be identified as parallel-offset synchronization regions. The corresponding 2D bifurcation plot is depicted in Fig. 9b to reveal the dynamical behaviors within the parallel-

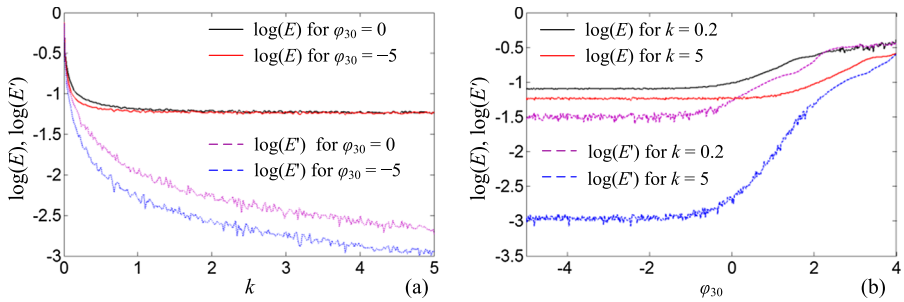

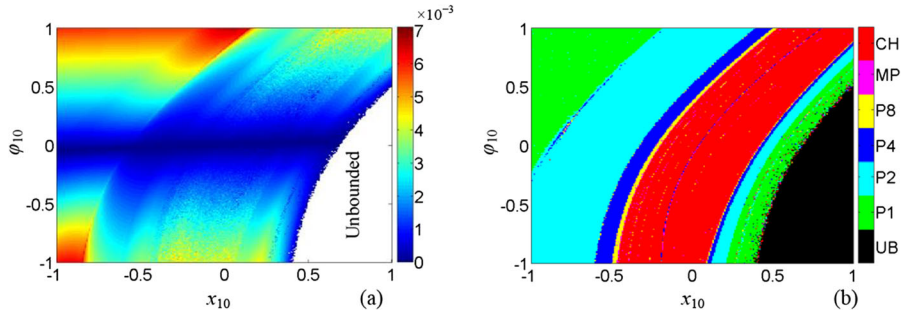

Fig.8 Normalized mean synchronization errors E and E' depicted concerning k or φ_{30} for (x_{10}, y_{10}, φ_{10}, x_{20}, y_{20}, φ_{20}) = (0.01, 0, 0.3, 0, 0, 0), **a** plots about variable k with fixed $\varphi_{30} = 0$ and $\varphi_{30} = -5$, **b** plots about variable φ_{30} with fixed $k = 0.2$ and $k = 5$

Fig. 9 Coexisting and synchronous dynamical behaviors in the x_{10}-φ_{10} plane with $k = 5$, $\varphi_{30} = -5$, and (x_{10}, y_{10}, φ_{10}, x_{20}, y_{20}, φ_{20}) = (x_{10}, 0, φ_{10}, 0, 0, 0), **a** normalized mean synchronization error E' in the x_{10}-φ_{10} plane, **b** 2D bifurcation plot in the $x_{10} - \varphi_{10}$ plane

offset synchronization regions. From these two figures, parallel-offset synchronized chaotic and periodic behaviors are discovered.

The phase portraits and time-domain waveforms of three representative synchronous behaviors of Figs. 7 and 9 are illustrated in Fig. 10a, b, respectively. In detail, Fig. 10a1, b1 shows the phase portraits and time waveforms for the completely synchronized periodic behavior occurring at $k = 0.2$ and (x_{10}, y_{10}, φ_{10}, x_{20}, y_{20}, φ_{20}, φ_{30}) = (− 0.5, 0, − 0.57, 0, 0, 0, 0). When $k = 5$, $\varphi_{30} = -5$ are assigned and the other initial conditions remain unchanged, the dynamics turns into parallel-offset synchronized periodic behavior as depicted in Fig. 10a2, b2. Furthermore, when $k = 5$ and $\varphi_{30} = -5$ remain unchanged and $x_{10} = 0.01$ and $\varphi_{10} = 0.3$ are specified, a parallel-offset synchronized chaotic behavior is obtained as shown in Fig. 10a3, b3. These results demonstrate that the synchronous behaviors of the memristor-coupled homogenous network are flexibly controlled by the coefficients of coupling memristor and the initial conditions of the two subsystems.

4.3 Phase synchronization

Phase synchronization can easily be achieved beyond the complete and parallel-offset synchronization regions. In this case, the phases of two subsystems become locked and their amplitudes remain highly uncorrelated [37]. Using the method described in [25], the phase of a periodic or chaotic motion can be defined as

$$\theta(t) = 2\pi n + 2\pi \frac{t - t_n}{t_{n+1} - t_n}, (t_n < t < t_{n+1}) \tag{12}$$

where t_n is the time of the n-th crossing of the motion on an appropriate Poincare section. Successive crossing with the Poincare section can be associated with a phase increase of 2π and the phases in between are computed with a linear interpolation as described in (12). Then, the phase synchronization can be identified by detecting the phase difference between two coupled subsystems.

The phase difference $\Delta\theta_1(t) = \theta_{x1}(t) - \theta_{x2}(t)$ calculated from the x_1 and x_2 components of network (2) is mainly examined. Its time-domain waveforms are

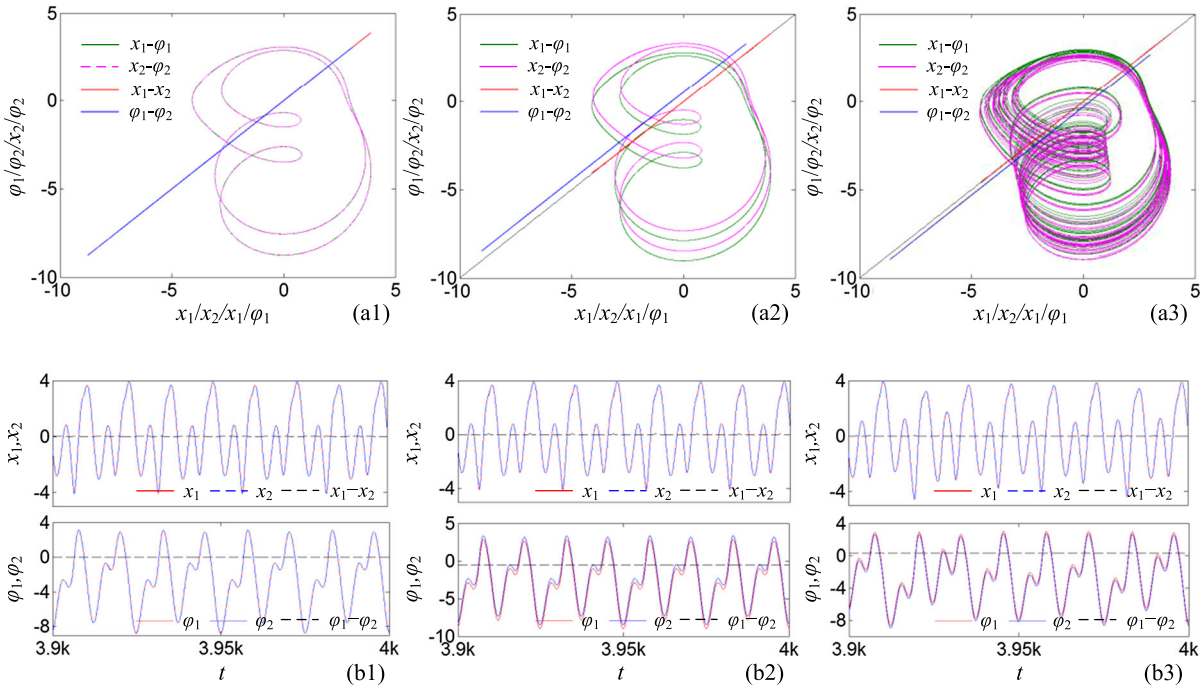

Fig.10 Phase portraits and time-domain waveforms of typical synchronous behaviors with varied k and initial conditions (x_{10}, y_{10}, φ_{10}, x_{20}, y_{20}, φ_{20}, φ_{30}) = (x_{10}, 0, φ_{10}, 0, 0, 0, φ_{30}), **a1** and **b1** complete synchronization for $k = 0.2$, $x_{10} = -0.5$, $\varphi_{10} = -0.57$, $\varphi_{30} = 0$, **a2** and **b2** parallel-offset synchronization for $k = 5$, $x_{10} = -0.5$, $\varphi_{10} = -0.57$, and $\varphi_{30} = -5$, **a3** and **b3** parallel-offset synchronization for $k = 5$, $x_{10} = 0.01$, $\varphi_{10} = 0.3$, and $\varphi_{30} = -5$

plotted under different sets of control parameters as shown in Fig. 11. Corresponding to the asynchronous motion depicted in Fig. 4c for $k = 0.2$ and (x_{10}, y_{10}, φ_{10}, x_{20}, y_{20}, φ_{20}, φ_{30}) = (0.01, 0, 0, 0, 0, 0, 3.5), the time evolution of phase difference $\Delta_1\theta(t)$ is depicted by a red line in Fig. 11a. The phase difference between x_1(t) and x_2(t) fluctuates around zero and the amplitudes of their trajectories are uncorrelated in most time regions, indicating the generation of phase synchronization. When $k = 0.2$ is assigned and the initial conditions are tuned as (0.01, 0, 1, 0, 0, 0, 0) and (− 1, 0, 1, 0, 0, 0, 0), the phase errors are illustrated by the green and black lines in Fig. 11a. The fluctuation amplitudes of phase errors are bounded within relatively small values and directed by the initial conditions of network (2). However, when y_1, y_2 or φ_1, φ_2 are taken as the analytic targets, the calculated phase differences $\Delta\theta_2(t) = \theta_{y1}(t) - \theta_{y2}(t)$ and $\Delta\theta_3(t) = \theta_{\varphi1}(t) - \theta_{\varphi2}(t)$ are slightly different from $\Delta\theta_1(t)$ as depicted in Fig. 11a. Their time-domain waveforms are illustrated in Fig. 11b, c, respectively. In summary, the natural frequencies of two subsystems are easily correlated due to the same stimulus of 1.8 cos(t) and their phase difference can be limited within an arbitrary constant.

When the stimulus frequency of the first subsystem is maintained as $F_1 = 1$ and that of the second subsystem is slightly increased to $F_2 = 1.01$, the frequency correlation breaks and the phases of the two subsystems become unlocked. The blue trajectory in Fig. 12a depicts the linearly decreased phase difference $\Delta\theta_1(t)$ for $k = 0.2$ and (x_{10}, y_{10}, φ_{10}, x_{20}, y_{20}, φ_{20}, φ_{30}) = (0.01, 0, 0, 0, 0, 0, 3.5). In this case, the two subsystems are asynchronous. If the coupling memristor coefficients are changed to $\varphi_{30} = -5$ and $k = 5$, the memristor-coupled network (2) enters an imperfect phase synchronization state with perfect synchronization epochs interrupted by regular phase slips. The corresponding time evolution of $\Delta\theta_1(t)$ is given at the bottom of Fig. 12a. In these two cases, the

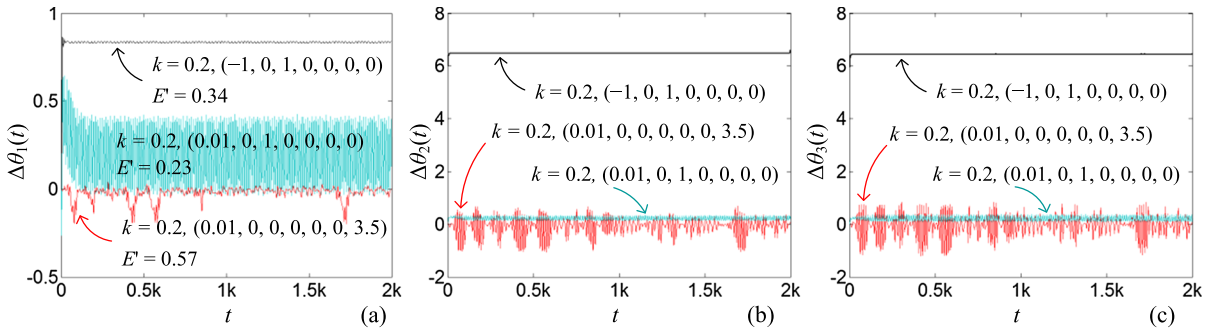

Fig. 11 Phase synchronization with the same stimulus frequency $F = 1$, **a** time evolutions of phase difference $\Delta\theta_1(t)$, **b** time evolutions of phase difference $\Delta\theta_2(t)$, **c** time evolutions of phase difference $\Delta\theta_3(t)$

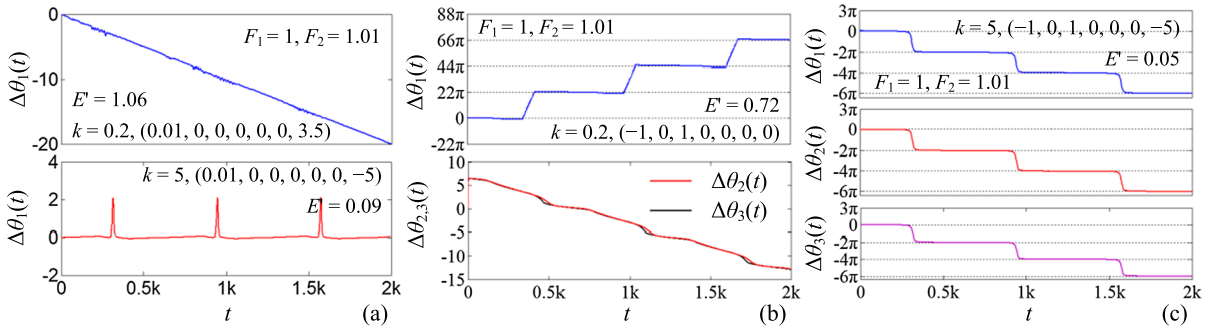

Fig. 12 Phase synchronization with different stimulus frequencies $F_1 = 1$ and $F_2 = 1.01$, **a** asynchronous motion and imperfect phase synchronization with regular phase slips, **b** imperfectly synchronized x_1 and x_2 state variables with 22π phase jumps, and asynchronous y_1, y_2, and φ_1, φ_2 state variables, **c** imperfect phase synchronization with -2π phase jumps

evolution patterns of $\Delta\theta_1(t)$, $\Delta\theta_2(t)$, and $\Delta\theta_3(t)$ are consistent.

In another case, we set $k = 0.2$ and $(x_{10}, y_{10}, \varphi_{10}, x_{20}, y_{20}, \varphi_{20}, \varphi_{30}) = (-1, 0, 1, 0, 0, 0, 0)$. The state variables x_1 and x_2 are imperfectly synchronized with 22π phase jumps, as shown by the blue line of Fig. 12b. However, the other two pairs of state variables are out of synchronization because their phase differences linearly decrease as depicted by the red and black lines of Fig. 12b. If φ_{30} and k are adjusted as -5 and 5, respectively, the whole network can reach imperfect phase synchronization and the amplitude of the phase jumps is reduced to 2π, as shown in Fig. 12c.

5 Circuit realization and PSIM simulations

In this section, the synchronous behaviors of the memristor-coupled network are equivalently verified in an analog circuit through PSIM circuit simulations. The PSIM software is commonly used to verify initial condition-sensitive dynamical behaviors [38, 39].

The implementation circuit of network (2) is designed as depicted in Fig. 13. It consists of seven integrators, an inverse addition circuit, four inverters, three hyperbolic tangent function converters, and four multipliers. The circuit equations for the seven capacitor voltages v_{x1}, v_{y1}, $v_{\varphi1}$, v_{x2}, v_{y2}, $v_{\varphi2}$, and $v_{\varphi3}$ are established as

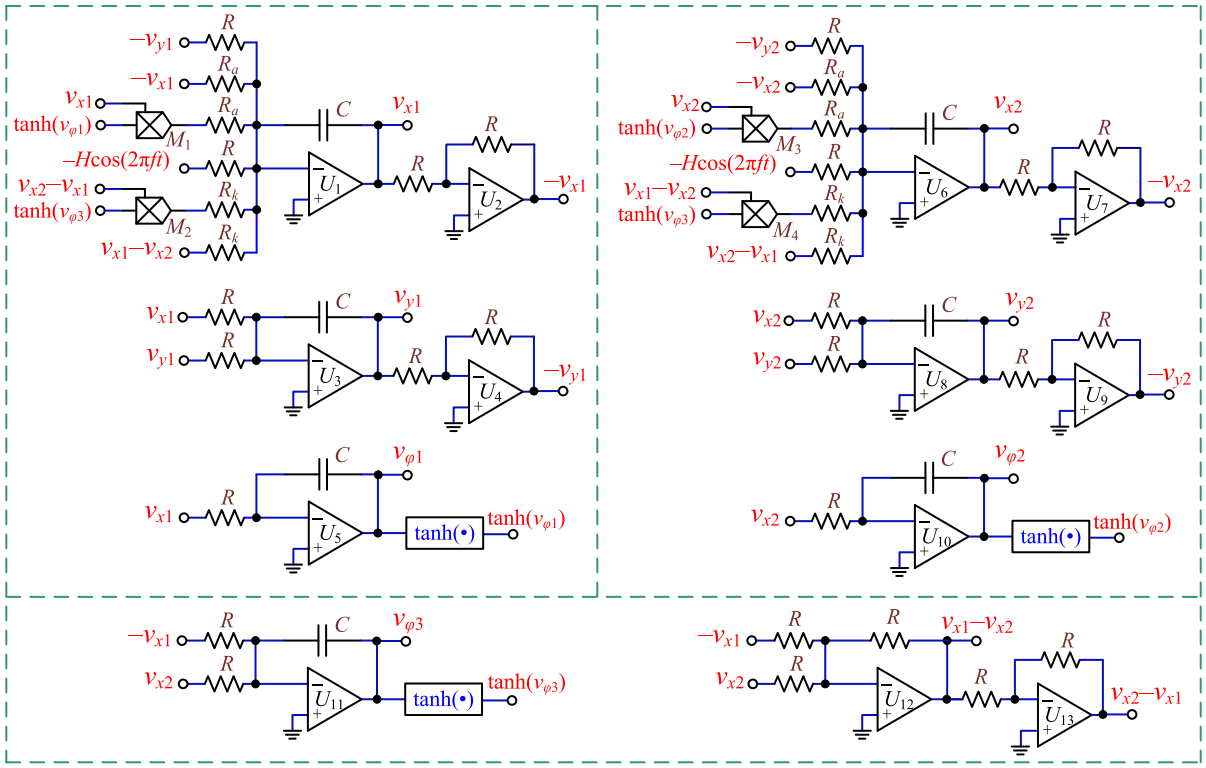

Fig. 13 Circuit schematics for the equivalent realization circuits of network (2)

$$\begin{cases} \mathrm{RC}\dfrac{\mathrm{d}v_{x1}}{\mathrm{d}t} = v_{y1} + \dfrac{R}{R_a}(1-\tanh v_{\varphi1})v_{x1} + 1.8\cos(2\pi ft) \\ \quad -\dfrac{R}{R_k}(1-\tanh v_{\varphi3})(v_{x1}-v_{x2}), \\ RC\dfrac{\mathrm{d}v_{y1}}{\mathrm{d}t} = -v_{x1} - v_{y1}, \\ RC\dfrac{\mathrm{d}v_{\varphi1}}{\mathrm{d}t} = -v_{x1}, \\ RC\dfrac{\mathrm{d}v_{x2}}{\mathrm{d}t} = v_{y2} + \dfrac{R}{R_a}(1-\tanh v_{\varphi2})v_{x2} + 1.8\cos(2\pi ft) \\ \quad +\dfrac{R}{R_k}(1-\tanh v_{\varphi3})(v_{x1}-v_{x2}), \\ RC\dfrac{\mathrm{d}v_{y2}}{\mathrm{d}t} = -v_{x2} - v_{y2}, \\ RC\dfrac{\mathrm{d}v_{\varphi2}}{\mathrm{d}t} = -v_{x2}, \\ RC\dfrac{\mathrm{d}v_{\varphi3}}{\mathrm{d}t} = v_{x1} - v_{x2}. \end{cases} \tag{13}$$

In Fig. 13, the gains of four multipliers M_1, M_2, M_3, and M_4 are set as 1. The time-constant-related circuit elements are optimized as $R = 10\,\mathrm{k\Omega}$ and $C = 100\,\mathrm{nF}$. Other circuit elements are calculated as $R_a = R/0.5 = 20\,\mathrm{k\Omega}$, $R_k = 10/k\,\mathrm{k\Omega}$, $f = F/(2\pi RC) = 159\,\mathrm{Hz}$. The memristor R_k and initial conditions of seven capacitor voltages $v_{x1}(0)$, $v_{y1}(0)$, $v_{\varphi1}(0)$, $v_{x2}(0)$, $v_{y2}(0)$, $v_{\varphi2}(0)$, and $v_{\varphi3}(0)$ are the main control parameters of this equivalent realization circuit.

Referring to Fig. 13, a circuit simulation model is established using PSIM software, in which the hyperbolic tangent function is realized by the editable math function modules. The simulation control parameters "time step", "total time", and "print time" are adjusted to 10 μs, 600 ms, and 400 ms, respectively. The three representative synchronous behaviors demonstrated in Fig. 10 are measured by adjusting R_k and seven initial capacitor voltages as $R_k = 50\,\mathrm{k\Omega}$, (− 0.5 V, 0 V, − 0.57 V, 0 V, 0 V, 0 V, 0 V), then as $R_k = 2\,\mathrm{k\Omega}$, (− 0.5 V, 0 V, − 0.57 V, 0 V, 0 V, 0 V, − 5 V), and finally as $R_k = 2\,\mathrm{k\Omega}$, (0.01 V, 0 V, 0.3 V, 0 V, 0 V, 0 V, − 5 V). The captured phase portraits and time-domain waveforms are presented in Fig. 14(a) and (b), respectively. The circuit simulation results in Fig. 14 agree well with the numerical simulation results in Fig. 10, implying the feasibility of the implementation circuit and verifying the

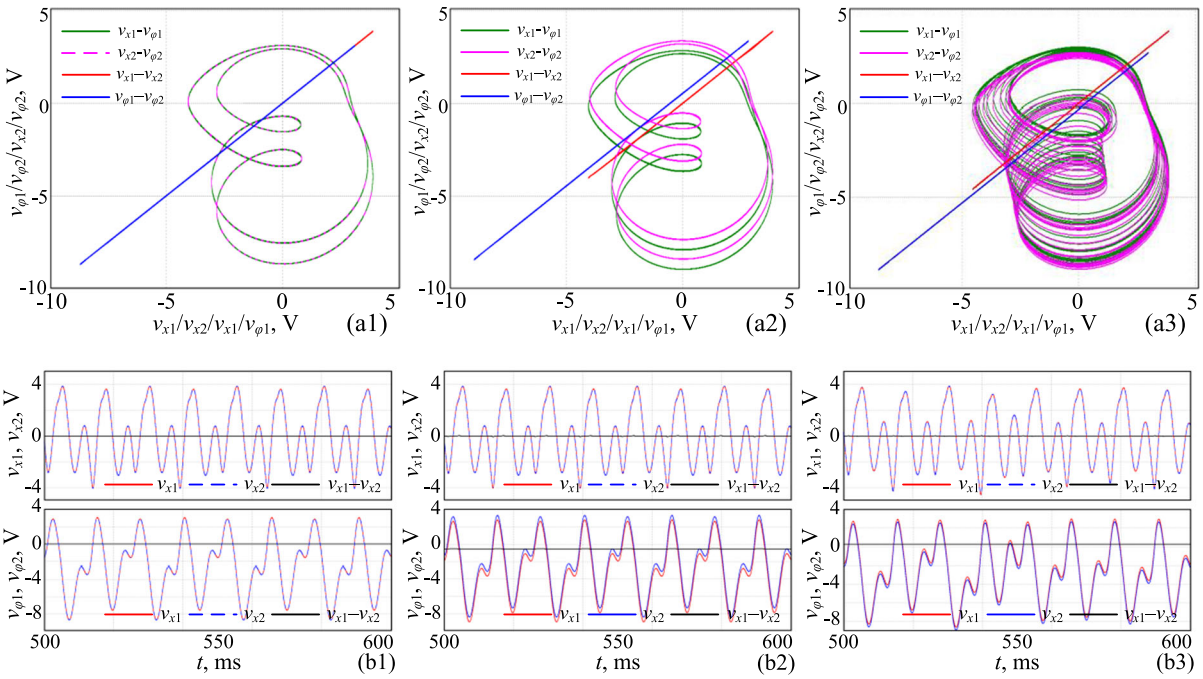

Fig. 14 PSIM circuit simulation results with fixed initial conditions $v_{y1}(0) = v_{x2}(0) = v_{y2}(0) = v_{\varphi 2}(0) = 0$ V, (a1) and (b1) complete synchronization for $R_k = 50$ kΩ, $v_{x1}(0) = -0.5$ V, $v_{\varphi 1}(0) = -0.57$ V, and $v_{\varphi 3}(0) = 0$ V, **a2** and **b2** Parallel-offset synchronization for $R_k = 2$ kΩ, $v_{x1}(0) = -0.5$ V, $v_{\varphi 1}(0) = -0.57$ V, and $v_{\varphi 3}(0) = -5$ V, **a3** and **b3** Parallel-offset synchronization for $R_k = 2$ kΩ, $v_{x1}(0) = 0.01$ V, $v_{\varphi 1}(0) = 0.3$ V, and $v_{\varphi 3}(0) = -5$ V

correctness of theoretical and numerical analysis results.

6 Conclusion

This work investigated the initial condition-sensitive coexisting and synchronous behaviors of a memristor-coupled homogeneous network consisting of two identical non-autonomous memristive Fitzhugh–Nagumo models. Affected by the external cosine stimuli, this homogenous network possesses a space equilibrium set $S = (0, 0, c_1, 0, 0, c_2, c_3)$ at discrete time points satisfying $1.8\cos(t) = 0$; otherwise, it has no equilibrium points. Similar to memristive systems with the line, plane, or space equilibrium sets, the memristor-coupled homogeneous network exhibits extreme multistability with coexisting hyperchaotic, chaotic, periodic, and quasi-periodic attractors. Moreover, a 4D dimensionality reduction model was built through incremental integral transformation, based on which the revealed extreme multistability phenomenon was proved to be hidden by stability analyses of the reformed equilibrium points. Numerical simulations demonstrated that the synchronicities of these coexisting hidden behaviors depend not only on the initial condition and coupling strength of the coupling memristor but also on the subsystems' initial conditions. When large positive coupling strengths and negative coupling memristor initial conditions are chosen, the two coupled Fitzhugh–Nagumo models can enter complete or parallel-offset synchronization states with properly selected subsystems' initial conditions. In addition to these two synchronous behaviors, phase synchronization can easily be achieved due to the existence of external stimuli. This initial condition-sensitive synchronization property can benefit the flexible control of the coupled homogeneous network.

In this study, only a pair of state variables is concerned in the coupling channel. The constructed network exhibits various coexisting and synchronous behaviors flexibly controlled by the coupling strength and initial conditions of the network. Future research will focus on introducing more than a pair of state variables in the coupling channel.

Acknowledgements This work was supported by the grants from the National Natural Science Foundation of China under Grant Nos. 52277001 and 12172066, the Qinglan Project of Jiangsu Province of China, the Postgraduate Research and Practice Innovation Program of Jiangsu Province, China, under Grant No. KYCX22_3052, and the College Students' Innovation and Entrepreneurship Training Program of Changzhou University.

Author contribution statement The authors contribute equally to this work.

Data Availability The datasets generated during and/or analyzed during the current study are available from the corresponding author on reasonable request.

Declarations

Conflict of interest The authors declare that they have no known competing financial interests or personal relationships that could have appeared to influence the work reported in this paper.

References

1. Chua, L.O.: If it's pinched it's a memristor. Semicond. Sci. Technol. **29**(10), 104001 (2014)
2. F. Corinto, M. Forti, L. O. Chua, Memristor circuits: Invariant manifolds, coexisting attractors, extreme multistability, and bifurcations without parameters, Nonlinear Circuits and Systems with Memristors, Springer, Cham, pp 219−269 (2021)
3. Volos, C.K., Pham, V.T., Nistazakis, H.E., Stouboulos, I.N.: A dream that has come true: Chaos from a nonlinear circuit with a real memristor. Int. J. Bifurcation Chaos **30**(13), 2030036 (2020)
4. Chen, M., Sun, M.X., Bao, H., Hu, Y.H., Bao, B.C.: Flux-charge analysis of two-memristor-based Chua's circuit: Dimensionality decreasing model for detecting extreme multistability. IEEE Trans. Ind. Electron. **67**(3), 2197–2206 (2020)
5. S. Q. Sun, D. W. Yan, M. Ji'e, X. Y. Du, L. D. Wang, S. K. Duan, Memristor-based time-delay chaotic system with hidden extreme multi-stability and pseudo-random sequence generator, Eur. Phys. J. Spec. Top. 230(18), 3481−3491 (2021)
6. Ma, J., Zhou, P., Ahmad, B., Ren, G.D., Wang, C.N.: Chaos and multi-scroll attractors in RCL-shunted junction coupled Jerk circuit connected by memristor. PLoS ONE **13**(1), e0191120 (2018)
7. S. Zhang, C. B. Li, J. H. Zheng, X. P. Wang, Z. G. Zeng, G. R. Chen, Generating any number of diversified hidden attractors via memristor coupling, IEEE Trans. Circuits Syst. I, Regul. Pap. 68(12), 4945−4956 (2021)
8. Chen, J.J., Yan, D.W., Duan, S.K., Wang, L.D.: Memristor-based hyper-chaotic circuit for image encryption. Chin. Phys. B **29**(11), 110504 (2020)
9. Xiu, C.B., Fang, J.Y., Liu, Y.X.: Design and circuit implementation of a novel 5D memristive CNN hyperchaotic system. Chaos, Solitons Fractals **158**, 112040 (2022)
10. Deng, Y., Li, Y.X.: A memristive conservative chaotic circuit consisting of a memristor and a capacitor. Chaos **30**(1), 013120 (2020)
11. Wang, Z., Qi, G.Y.: Modeling and analysis of a three-terminal-memristor-based conservative chaotic system. Entropy **23**(1), 71 (2021)
12. Huang, Y.C., Liu, J.X., Harkin, J., McDaid, L., Luo, Y.L.: An memristor-based synapse implementation using BCM learning rule. Neurocomputing **423**, 336–342 (2021)
13. X. X. Yang, B. Taylor, A. L. Wu, Y. R. Chen, L. O. Chua, Research progress on memristor: from synapses to computing systems, IEEE Trans. Circuits Syst. I, Regul. Pap. 69(5), 1845−1857 (2022)
14. Lin, H.R., Wang, C.H., Deng, Q.L., Xu, C., Deng, Z.K., Zhou, C.: Review on chaotic dynamics of memristive neuron and neural network. Nonlinear Dyn. **106**(1), 959–973 (2021)
15. Zhu, X., Wang, Q., Lu, W.D.: Memristor networks for real-time neural activity analysis. Nat. Commun. **11**(1), 2439 (2020)
16. Pisarchik, A.N., Jaimes-Reátegui, R., Rodríguez-Flores, C., García-López, J.H., Huerta-Cuéllar, G., Martín-Pasquín, F.J.: Secure chaotic communication based on extreme multistability. J. Franklin Inst. **358**(4), 2561–2575 (2021)
17. Fang, S.T., Zhou, S.X., Yurchenko, D., Yang, T., Liao, W.H.: Multistability phenomenon in signal processing, energy harvesting, composite structures, and metamaterials: a review. Mech. Syst. Sig. Process. **166**, 108419 (2022)
18. Lai, Q., Wan, Z.Q., Kuate, P.D.K., Fotsin, H.: Coexisting attractors, circuit implementation and synchronization control of a new chaotic system evolved from the simplest memristor chaotic circuit. Commun. Nonlinear Sci. Numer. Simul. **89**, 105341 (2020)
19. Mathiyalagan, K., Sangeetha, G.: Second-order sliding mode control for nonlinear fractional-order systems. Appl. Math. Comput. **383**, 125264 (2020)
20. Yang, Z., Luo, B., Liu, D., Li, Y.: Adaptive synchronization of delayed memristive neural networks with unknown parameters. IEEE Trans. Syst. Man Cybern. Syst. **50**(2), 539–549 (2020)
21. Li, R.H., Wu, H.Q., Cao, J.D.: Exponential synchronization for variable-order fractional discontinuous complex dynamical networks with short memory via impulsive control. Neural Netw. **148**, 13–22 (2022)
22. Gambuzza, L.V., Buscarino, A., Fortuna, L., Frasca, M.: Memristor-based adaptive coupling for consensus and synchronization. IEEE Trans Circuits Syst. I Regul. Pap. **62**(4), 1175–1184 (2015)
23. Zhang, X., Wu, F., Ma, J., Hobiny, A., Alzahrani, F., Ren, G.: Field coupling synchronization between chaotic circuits via a memristor. AEU Int. J. Electron. Commun. **115**, 153050 (2020)
24. Marković, D.: Synchronization by memristors. Nat. Mater. **21**(1), 4–5 (2022)
25. Li, Z., Zhou, H., Wang, M., Ma, M.: Coexisting firing patterns and phase synchronization in locally active memristor coupled neurons with HR and FN models. Nonlinear Dyn. **104**(2), 1455–1473 (2021)

26. Xu, Q., Liu, T., Ding, S.K., Bao, H., Li, Z., Chen, B.: Extreme multistability and phase synchronization in a heterogeneous bi-neuron Rulkov network with memristive electromagnetic induction. Cogn. Neurodyn. (2022). https://doi.org/10.1007/s11571-022-09866-3
27. Bao, H., Zhang, Y., Liu, W., Bao, B.C.: Memristor synapse-coupled memristive neuron network: synchronization transition and occurrence of chimera. Nonlinear Dyn. **100**(1), 937–950 (2020)
28. Bao, B.C., Yang, Q.F., Zhu, D., Zhang, Y.Z., Xu, Q., Chen, M.: Initial-induced coexisting and synchronous firing activities in memristor synapse-coupled Morris-Lecar bi-neuron network. Nonlinear Dyn. **99**(3), 2339–2354 (2020)
29. Korneev, I.A., Semenov, V.V., Slepnev, A.V., Vadivasova, T.E.: The impact of memristive coupling initial states on travelling waves in an ensemble of the FitzHugh–Nagumo oscillators. Chaos Solitons Fractals **147**, 110923 (2021)
30. Zhang, S., Li, C.B., Zheng, J.H., Wang, X.P., Zeng, Z.G., Peng, X.P.: Generating any number of initial offset-boosted coexisting Chua's double-scroll attractors via piecewise-nonlinear memristor. IEEE Trans. Ind. Electron. **69**(7), 7202–7212 (2021)
31. Zhang, J., Liao, X.F.: Effects of initial conditions on the synchronization of the coupled memristor neural circuits. Nonlinear Dyn. **95**(2), 1269–1282 (2019)
32. Bao, H., Liu, W.B., Chen, M.: Hidden extreme multistability and dimensionality reduction analysis for an improved non-autonomous memristive FitzHugh–Nagumo circuit. Nonlinear Dyn. **96**(3), 1879–1894 (2019)
33. Chen, M., Wang, C., Wu, H.G., Xu, Q., Bao, B.C.: A non-autonomous conservative system and its reconstitution in integral domain. Nonlinear Dyn. **103**(1), 643–655 (2021)
34. Doubla, I.S., Ramakrishnan, B., Njitacke, Z.T., Kengne, J., Rajagopal, K.: Hidden extreme multistability and its control with selection of a desired attractor in a non-autonomous Hopfield neuron. AEU Int. J. Electron. Commun. **144**, 154059 (2022)
35. Parastesh, F., Azarnoush, H., Jafari, S., Hatef, B., Perc, M., Repnik, R.: Synchronizability of two neurons with switching in the coupling. Appl. Math. Comput. **350**, 217–223 (2019)
36. Ren, X., Chen, B., Xu, Q., Wu, H.G., Chen, M.: Parameter and initial offset boosting dynamics in two-memristor-based Colpitts system. Eur. Phys. J. Spec. Top. **230**(7), 1709–1721 (2021)
37. Boccaletti, S., Kurths, J., Osipov, G., Valladares, D.L., Zhou, C.S.: The synchronization of chaotic systems. Phys. Rep. **366**(1), 1–101 (2002)
38. Chen, B., Cheng, X.X., Wu, H.G., Bao, B.C., Xu, Q.: Infinitely many necklace-shaped coexisting attractors in a nonautonomous memcapacitive oscillator. Int. J. Bifurcation Chaos **32**(02), 2250028 (2022)
39. Xie, W.L., Wang, C.H., Lin, H.R.: A fractional-order multistable locally active memristor and its chaotic system with transient transition, state jump. Nonlinear Dyn. **104**(4), 4523–4541 (2021)